Localized Nanogap Plasmonics: Extreme nanophotonics from ultrathin metallic gaps

Jeremy J. Baumberg[*,1], *Javier Aizpurua*[2], *Maiken H. Mikkelsen*[3] *and David R. Smith*[3]

[1] *NanoPhotonics Centre, Cavendish Laboratory, University of Cambridge, Cambridge, CB3 0HE, UK*
[2] *Materials Physics Center CSIC-UPV/EHU and Donostia International Physics Center DIPC, Paseo Manuel de Lardizabal, 20018 Donostia-San Sebastiàn, Spain*
[3] *Center for Metamaterials and Integrated Plasmonics, Duke University, Durham, North Carolina 27708, United States*

ABSTRACT:
Ultrathin dielectric gaps between metals can trap plasmonic optical modes with surprisingly low loss and with volumes below 1nm^3. We review the origin and subtle properties of these modes, and show how they can be well accounted for by simple models. Particularly important is the mixing between radiating antenna and confined nanogap modes, which is extremely sensitive to precise nano-geometry, right down to the single atom level. Coupling nanogap plasmons to electronic and vibronic transitions yields a host of phenomena including single-molecule strong coupling and molecular optomechanics, opening access to atomic-scale chemistry and material science, and quantum metamaterials. Ultimate low-energy devices such as robust bottom-up assembled single-atom switches are thus in prospect.

Because they couple optical fields with electronic excitations, plasmonic nanostructures confine light to dimensions far smaller than the free-space wavelength. Highlighted since the earliest studies[1], interest in the 1990s grew when local fields around nanostructures could be directly measured by near-field scanning optical microscopy[2,3]. Plasmon nanostructures gained rapid appreciation as routes to optical devices unconstrained by the wavelength of light, yielding viable *nanophotonic* devices[4–6].

A metallic nanoparticle of gold, silver, copper or aluminium exhibits plasmon resonances at wavelengths determined by its material properties, shape, and size. For metallic nanoparticles with sharp corners or protrusions, light can be strongly localized to volumes with minimum dimensions of 10-100 nm [7–10]. Achieving even more tightly confined fields on the scale of 1 nm or less, is possible but very difficult with single nanoparticles, since neither colloidal nor lithographic fabrication approaches offer reproducible control over such small feature sizes. Many advanced optical phenomena however hinge on such tightly localized fields, and require the strongest field enhancements and localization possible, for instance to elicit surface-enhanced Raman scattering[11] (SERS) or photon blockade from single molecules.

* jjb12@cam.ac.uk

Coupling nanoparticle plasmons together represents an alternative approach to field localization, as light can be tightly confined to the gaps between nanoparticles[12–14]. However, the same limitations in fabrication capabilities also lead to inconsistent control over gap dimensions in nanoparticle clusters[15].

Fortunately, the large field enhancements associated with nanoparticle clusters can also be achieved with single nanoparticles separated from a metal film by a thin dielectric layer, which behave similarly to a pair or *dimer* of nanoparticles[16–18]. In one realisation for UHV environments, the gaps between scanning probe tips and metallic surfaces can produce well-controlled cavities where single molecule spectroscopy is possible[19] (TERS). Although this plasmonic environment is less controlled than alternatives discussed below, it is capable of electrical excitation and high spatial resolutions[20–22] while other scanning systems have also been created by adhering or fabricating metal nanostructures onto AFM tips or optical fibres[23]. However for robust devices, the initial approach of top-down lithographic definition of gaps[24,25] has more recently been complemented by bottom-up self-assembly, which provides exquisitely-defined gaps down to 0.3 nm [26–28].

The 'gap plasmons' confined between two opposing metal surfaces propagate similarly to a wave along a transmission line[29,30]. These gap modes have complex behaviours and enter the regime of 'extreme nano-optics' because they can be sensitive to single atom placements. This geometry, which has been known variously as a 'nano-patch optical antenna', 'nanoparticle-on-mirror (NPoM)', 'metal-insulator-metal (MIM) waveguide', or 'particle over surface', has become increasingly studied for a wide variety of optical phenomena. The attractiveness of the plasmonic nano-patch or NPoM stems from its ease of fabrication combined with the extreme field enhancements available in either colloidal or lithographically patterned systems. The plasmonic nano-patch has proven a remarkably successful and robust platform for demonstrating a wide variety of optical phenomena. In this review, we focus specifically on the nano-patch, providing intuitive interpretations of its properties and exploring its use across different application areas.

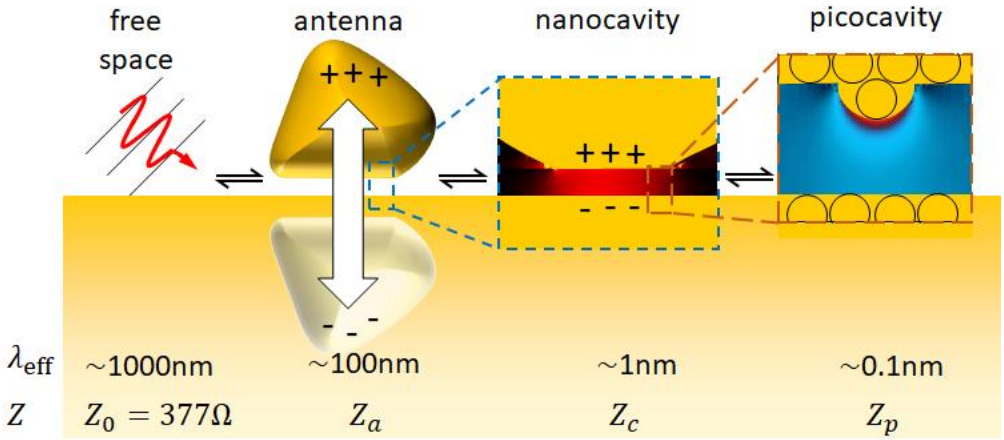

Figure 1 | Impedance matched coupling of light from free space to atomic scale. Schematic of cascade of effective wavelength scales between free-space photons, coupled via antennas into nanogap modes, which can then couple to atomic-scale protrusions ('picocavities').

Recent demonstrations that light can be trapped in optical modes of nanogaps with rigorously-defined mode volumes below 1nm^3 from surface atoms[31] shows why nanogap

plasmons are so important. Every gold surface supports adatoms, but normally the tight confinement into atomic-scale modes leads to negligible interaction with free-space photons. Only due to impedance matching of the plasmonic antennas and nanogaps to free space is it now possible to couple into and out of these highly-localized modes with high efficiencies >10% (FIG.1). As a simple initial estimate, the effective impedance of a nanoantenna scales with the current dipole length (ℓ) as[32] $Z_r = Z_0(\ell/\lambda)^2$ and hence the typical power coupling efficiency into an atomically-localized plasmon is $4(\ell/\lambda)^2 \sim 10^{-6}$. When there are intermediate stages through successively tighter-confined plasmon modes (FIG.1), this coupling can be improved by five orders of magnitude. Optimising antenna coupling is crucial for utilization in optoelectronic devices[33,34].

Basic concepts in plasmonic gap modes

To discuss the plasmonic gap modes, we first consider an infinite planar MIM multilayer[35,36]. For small gaps (d<10nm) of dielectric permittivity $\varepsilon_g = n_g^2$ between metallic walls (ε_m), the dispersion relation of the lowest MIM modes can be written analytically[37,38]

$$(k_\parallel/k_0)^2 = n_{\text{eff}}^2 = \varepsilon_g + 2\zeta\left[1 + \sqrt{1 + (\varepsilon_g - \varepsilon_m)/\zeta}\right] \quad (1)$$

with

$$\zeta = \left(k_0\, d\, \varepsilon_m/\varepsilon_g\right)^{-2} \quad (2)$$

which for typical nanogap parameters possess high wavevectors ($k_\parallel$=10-100 k_0 with $k_0 = 2\pi/\lambda$) and thus short effective wavelengths (FIG.2a). These gap plasmon modes are robust against attenuation because when their in-plane wavevector increases with decreasing gap, the imaginary out-of-plane wavevector must also increase to ensure $k_0^2 = k_\parallel^2 + k_\perp^2$, with a resulting field penetration depth

$$\delta_\perp = \frac{1}{\Im\mathrm{m}\{k_\perp\}} = \frac{d}{2\varepsilon_g\, \Re\mathrm{e}\{1/\varepsilon_m\}} \quad (3)$$

that correspondingly decreases[39]. As a result the loss per unit length for MIM plasmons remains unchanged as the gap decreases (they travel slower, but retract from the metal, as similarly shown for monolayer metals such as graphene[40]).

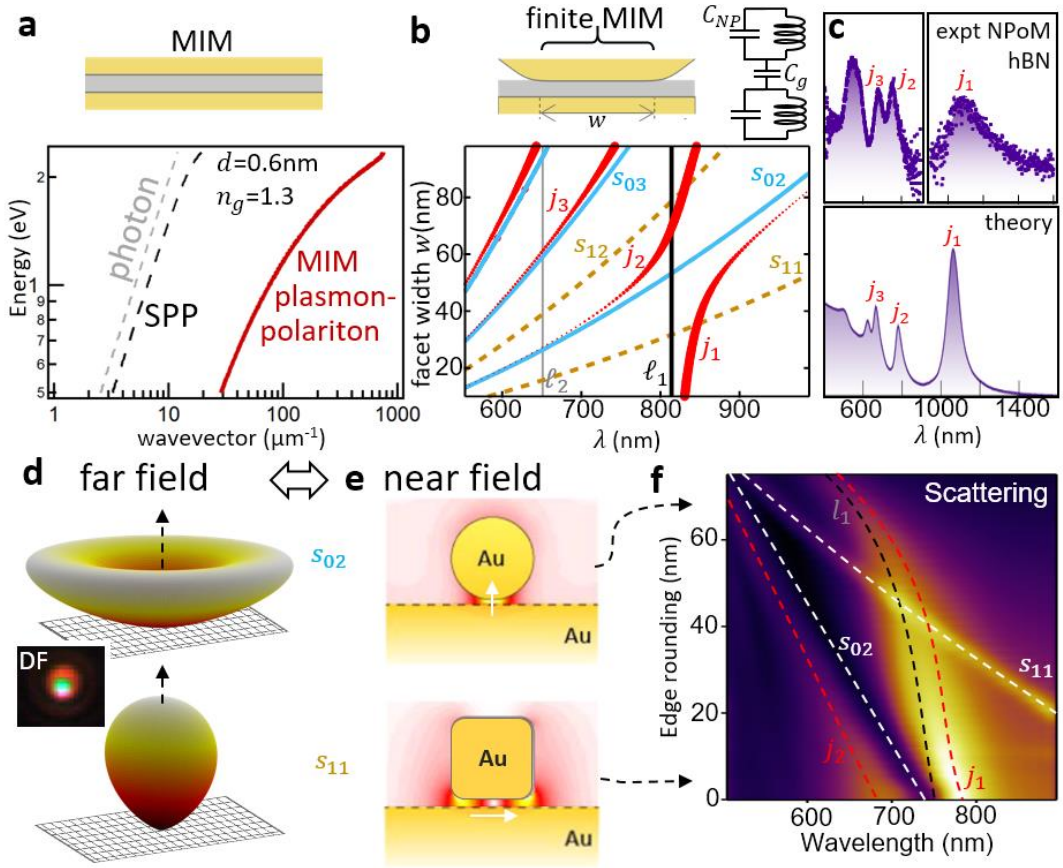

Figure 2 | Nanogap modes. a | Mode dispersion of plasmon-polariton in 2D infinite MIM structure. **b** | Finite bounded nanogap gives gap modes s_{mn} seen in scattering spectra that tune with facet width w in a flat-junction NPoM configuration. Equivalent circuit shows coupled antenna mode l=1. **c** | Experimental and theoretical scattering spectra for 80 nm NPoM on monolayer of hBN. **d** | Angular emission patterns (inset shows real space red ring for s_{02} z-polarised emission), with **e** | near-field distributions of s_{02} (top) and s_{11} (bottom) modes, white arrows show gap field orientation. **f** | Far-field emission (d=3nm, 2R=75nm) as cube is morphed to spherical nanoparticle on mirror, showing mixed modes j_i.

This continuum of MIM gap modes is broken into discrete states by the shape of the particle's facets which localize the modes at the finite gap. A simple 2D Fabry-Perot resonator model given by the partial reflection of plasmons at the discontinuities of the MIM gap from each lower facet edge serves to capture the nature and symmetry of the modes sustained. For facet width w, the discrete wavelengths are then[39,41]

$$\lambda_i^s = \frac{\pi}{\alpha_i} w\, n_{\text{eff}}(\lambda) \;\simeq\; \lambda_p \sqrt{\frac{w\varepsilon_g}{d\alpha_i} + \varepsilon_\infty} \qquad (4)$$

where α_i are the zeros of the first Bessel function (assuming here 2D circular symmetry), and where a Drude metal permittivity $\varepsilon_m = \varepsilon_\infty - \lambda^2/\lambda_p^2$ with dielectric background ε_∞, and plasma wavelength λ_p is used (for Au λ_p~148nm). This set of modes spans the visible and near-infrared as the MIM facet or patch size w is varied (FIG.2b). More generally these tune also with the precise 2D facet shape thus giving gap modes s_{mn} where indices m, n indicate the number of nodes in radial and azimuthal directions.[42] With such small effective wavelengths, these modes have very poor direct coupling efficiency to free space (of order 10^{-4}).

However the gap modes are able to couple to plasmonic antenna modes that span the entire nanoparticle-substrate system (FIG.1a), and this greatly increases their coupling. Antenna mode wavelengths can be estimated using simple circuit models, which assume quasi-static field response in such small sub-wavelength resonators[43–45]. These treat each individual nano-component as lumped LCR resonators (FIG.2b), which are then capacitively coupled by the gap, C_g, to give the lowest antenna mode (l=1) [46]

$$\lambda_1^l = \lambda_p \sqrt{\varepsilon_\infty + 2\varepsilon_d + 4\varepsilon_d C_g / C_{NP}} \quad (5)$$

where ε_d is the permittivity of the dielectric medium in which the system is embedded, and the capacitance of the nanoparticle/structure is C_{NP} ($2\pi R\varepsilon_0$ for a sphere of radius R, with corresponding expressions for cubes or plates). This formula works for patterned multilayers, dimers, nanopatches or nanoparticles on a surface[47], using the appropriate $C_{g,NP}$, and scales with the height of the nanoparticle because charges oscillate across the entire structure (FIG.1). For dimers or spherical NPoMs,[46] $C_g = C_{NP}\,\varepsilon_g^{\chi} \ln[1 + \varsigma R/d]$ with constants $\chi \sim 0.5, \varsigma \sim 0.15$ for the NPoM, giving characteristic red-shifts with decreasing gap and increasing NP size:

$$\left(\lambda_1^l/\lambda_p\right)^2 = \varepsilon_\infty + 2\varepsilon_d + 4\varepsilon_d \varepsilon_g^{\chi} \ln[1 + \varsigma R/d]. \quad (6)$$

The next order (l=2) antenna mode is shifted to shorter wavelengths by a factor ~1.25, set by the charge distributions that give the gap capacitance. Coupling strengths from free space to the antenna mode follow as R^3 as expected from quasistatic dipole coupling to the entire NP volume[47].

Antenna modes l with the correct symmetry can couple to specific MIM gap plasmons s_{mn}, typically yielding strong anticrossings (FIG.2b) and mixed $s_{mn} + l = j_n$ modes. It is around these anticrossings between λ^l and λ_{mn}^s that light is most efficiently coupled into the nanogaps[41] (FIG.2c). However the antenna-nanogap coupling depends exquisitely on the shape of the facet edges, as well as the mode symmetries, since facet edge morphology on the scale of $1/k_{\parallel}$~1nm controls how easily gap plasmon fields reach around to the upper surfaces of the NP where antenna modes are located. Similar considerations obtain for modes of the cube-on-mirror[48], which depend also on facet edge shapes. In larger gaps (d>5nm) MIM cavity nanogap modes with odd m (such as s_{11}) which support in-plane optical fields are found in the near-infrared (NIR), however for smaller gaps these rapidly tune further into the infrared (λ_{11}^s>1μm). By contrast, modes with even m possess strongest vertical (perpendicular) optical fields in the gap (s_{02}) and remain in the vis-NIR even for the smallest gaps. Gap modes that do not mix with the antenna modes form dark modes[49].

Different dipole-type emission patterns (FIG.2d) arise from the different field orientations in the nanogap (FIG.2e). In-plane modes present for larger gaps radiate normal to the substrate (85% collected by NA 0.9). By contrast, vertically polarised gap modes radiate symmetrically at high angles, $I(\theta) \propto \left|1 + r_p\right|^2 \sin^2\theta$ (where $r_p(\theta)$ is the Fresnel factor for p-polarised light) giving maximum emission at ~60° in a FWHM 10° (with 55% thus collected by NA 0.9), which is radially polarised and focusses to a real-space ring (FIG.2d inset). For real facets which are asymmetrically shaped, more complex polarisation-dependent scattering spectra are observed, involving several split modes[42,50]. The different mode tuning with facet size can be seen by morphing a spherical NP into a nanocube[51] of the same

height (FIG.2f), showing how the antenna mode crosses the in-plane field mode s_{11} (different symmetry), while anticrossing the vertical field mode s_{02}. The antenna modes themselves also tune weakly with nano-geometry, leading to complex optimisations to retain best resonance conditions.

The maximum field enhancements E in the gap increase strongly as the gap size shrinks (which is important for the Purcell factor, see below), and here we provide an approximate formula for this. For small gaps (<5nm), the vertical field is uniform across the gap. The lateral localisation of the intensity within the gap has a spatial FWHM $\Delta x = \sqrt{2Rd/\varepsilon_d}$ with this model matching simulations.[52] Incident light E_0 excites the spherical nanoparticle antenna dipole with polarizability $\alpha = 4\pi R^3 \chi$ where $\chi = \frac{\varepsilon_m - \varepsilon_s}{\varepsilon_m + 2\varepsilon_s} \sim 2$ for Au in air near λ_1^l. Incoming energy $\frac{1}{2}\varepsilon_0 \alpha E_0^2$ is then concentrated into the nanogap mode of volume $V_I = d\,\pi\Delta x^2/4\ln 2 = \frac{\pi R d^2}{2\ln 2\, n_g^2}$. This contains the equivalent energy $\frac{1}{2}\varepsilon_0 \varepsilon_g V_I\, E_{\max}^2$ that is boosted by the Q-factor of the resonance Q∼15. Combining these yields an estimate of the field enhancement

$$\frac{E_{\max}^2}{E_0^2} = (16\ln 2)\,\mathrm{Q}\, n_g \frac{R^2}{d^2} \tag{7}$$

corresponding well with full simulations in the small gap limit. Field enhancements exceeding 600 are thus possible in nm-scale gaps, but depend greatly on the exact morphology. The effective volume of a mode is one of the key parameters that governs light-matter interactions and this V_W can be rigorously extracted from full simulations[53], as it is related to field enhancement and spatial localization. These give $V_W \propto d^{2.5}$ independent of R, slightly different from V_I since field penetration in the metal is included (which roughly doubles the mode volume). These small gaps thus give rise to enormously-enhanced interactions between light and electronic excitations ($\propto 1/\sqrt{V_W}$) and light and phonons ($\propto 1/V_W$), discussed below.

As a result of all the considerations above, great care has to be taken in understanding the modes, their spectral positions, couplings and their field enhancements for the different specific applications. We highlight that the permittivity of the spacer in the gap is rarely isotropic (for instance graphene, transition-metal dichalcogenides (TMDs), hyperbolic phononic materials such as hBN, or oriented molecules), and this also plays a role in tuning the modes and enhancements since then the ε_g employed in Eqs. (1-5) depends on the optical field directions of the gap plasmons involved.

As noted above, scanning-tunnelling microscopy also produces nanogaps, which can be spatially scanned. While the nanogap modes defined between tip and metallic substrate are similar to those above, their out-coupling is not typically well defined because of the lack of antenna modes. This can be ameliorated by shaping a neck on the tip[54], using grating coupling[55], coupling directly in the near-field to polariton modes[34], or from the random metallic grain structure on the end of typical tips (hence the occasional 'magic tips' found).

Remarkably, additional confinement can be provided by individual atomic protrusions into the gap. Time-dependent density functional theory (TDDFT) for small NPs confirms[31,56,57] that even single atoms can provide up to fivefold further local electromagnetic

enhancement (on top of the plasmonic background field) leading to local fields more than a thousand times the incident field (FIG.1). Intriguingly, classical electromagnetic calculations give very similar results, with protrusions of aspect ratio $a = \cos\phi$ leading to extra enhancements $E_{\text{pico}} = \sin^2\phi\,/(1-\phi/\tan\phi) \simeq 1 + 1.7a + 0.3a^2$, of order ~3 for single atom protrusions[58]. This effect is akin to the lightening rod effect which is thus found to operate on the atomic scale, and produces cavity volumes $V_W < 1\text{nm}^3$ which are thus termed 'picocavities', and recently shown experimentally to be induced by optical irradiation[31].

Light-matter electronic interactions in nanogaps

Emitters placed in the enhanced fields of such ultrathin metallic junctions experience modified absorption and emission rates, quantum efficiencies, and radiation patterns, which can lead to strong coupling. A wide variety of materials can be integrated, including quantum dots[59,60], mono- and few-layer transition metal dichalcogenides[61,62] and fluorescent dyes[63,64] (FIG.3a). The nanoscale spatial position of the emitter and orientation of its dipole moment is crucially important since the local fields of nanogap structures can vary significantly across ~10 nm and couple preferentially to one orientation of the dipole ($\boldsymbol{p}$). To achieve this level of control, precision methods such as DNA origami can selectively position dye molecules (DNAo:dye)[65] or barrel-shaped non-fluorescing molecules such as cucubit[n]urils (CB[n]s) can be used to orient dye molecules of interest (CB:dye)[66].

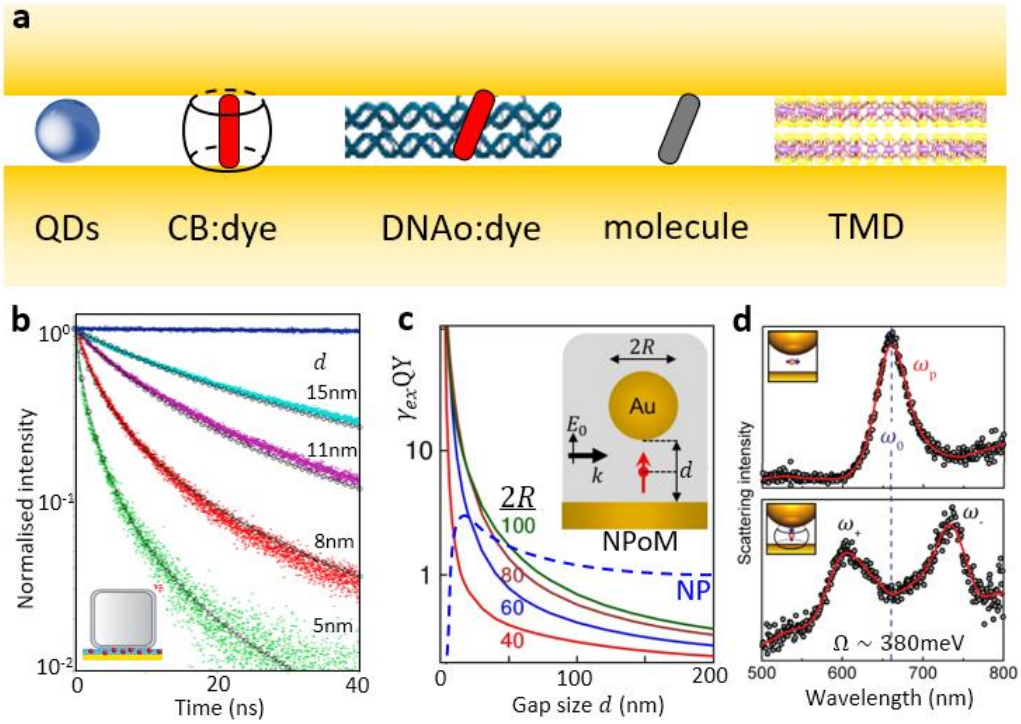

Figure 3 | Emitters in nanocavities. a | Emitter types include quantum dots (QDs), dye molecules supported by CB or DNA scaffolds, organic molecules, and monolayer materials (graphene, TMDs, hBN). **b** | Emission intensity decay for dyes in high Purcell factor cube-on-mirror vs gap size. **c** | Radiative yield of a single emitter in the gap centre of a plasmonic gold nanoparticle-on-mirror as a function of gap size, comparing single NP and NPoM. **d** | Strong coupling for 3 emitters in NPoM of configuration **c** with d=0.9nm gap.

An important question that arises for emitters in close proximity to plasmonic structures is whether the fluorescence is increased due to the high local field intensity or decreased due to non-radiative decay channels introduced by the metal. Large fluorescence enhancements of emitters coupled to plasmonic nanogap structures are observed[67] (in some cases exceeding 30,000-fold[63]), however quenching and reduced fluorescence have also been reported. Both scenarios indeed occur in seemingly similar structures, as the radiative and non-radiative decay rates depend intricately on the geometry and dimensions of the nanogap structure, the placement and initial quantum yield of emitters within it, and excitation conditions. Fluorescence changes come from modified radiative quantum yields (QY, the probability that relaxation results in an emitted photon), and altered efficiencies of excitation (γ_{ex}) and collection (η) due to the antenna behaviour of plasmonic structures. Additionally, for high excitation powers at or near saturation, enhanced spontaneous emission rates (γ_{sp}) enable the emitter to be re-excited after a shorter amount of time, also contributing to fluorescence enhancement. The fluorescence observed from an emitter coupled to a plasmonic structure compared to a control sample (denoted by superscript 0) is enhanced by a factor $EF = \gamma_{\mathrm{tot}}/\gamma_{\mathrm{tot}}^{0}$ (where $\gamma_{\mathrm{tot}} = \eta\gamma_{ex}\gamma_{sp}\mathrm{QY}$), and the contribution from the increase in γ_{sp} should only be considered for excitation at or near saturation. The enhancement in excitation rate arises from $\gamma_{ex} \propto |\boldsymbol{p} \cdot \boldsymbol{E}|^2$ for $\boldsymbol{E}$ at the emitter's position and transition frequency. If the QY is initially close to 100% it can only be decreased, but for emitters with lower QY such as infrared emitters[68] and certain molecules, the QY can be increased significantly. Observation of fluorescence enhancement should thus not be attributed to either enhanced QY or enhanced spontaneous emission alone. Rather, a careful analysis is required of the interplay between the multiple contributing factors.

Tailoring the spontaneous emission rate of emitters by embedding them inside cavities offers the promise of ultrafast low-power light sources, modulators and single photon sources. The (intrinsic) dipole moment and controllable electromagnetic environment of an emitter determines its spontaneous emission rate, $\gamma_{sp} \propto |\boldsymbol{p}|^2\rho$, where ρ is the local density of optical states at the position and frequency of the emitter, which can be obtained from Green's function approaches[69–71]. This electromagnetic environment is modified by high-quality-factor dielectric cavities or plasmonic structures with ultrasmall mode volumes as discussed here. An emitter then experiences an increased spontaneous decay rate compared to free space, with the ratio $F_P = \gamma_{sp}/\gamma_{sp}^{0}$ known as the Purcell factor. The spontaneous decay rate, $\gamma_{sp} = \gamma_r + \gamma_{nr}$, has contributions from both radiative decay, γ_r, and non-radiative decay, γ_{nr} which includes generation of surface or localized modes and thermal dissipation. As the non-radiative decay rates can be significant for plasmonic structures, the enhancement in radiative rate γ_r/γ_r^{0} where $\gamma_r = \gamma_{sp}\mathrm{QY}$ is often of greater interest[72], which requires fluorescence lifetime measurements and careful analysis to properly extract.

Balancing the trade-off between high field enhancements and non-radiative decay allows the observation of large radiative-rate enhancements ~1000 for dye molecules embedded in a 10 nm gap between a metal film and silver nanocubes or nanowires[73] or within a NPoM formed by DNA origami[65]. This spontaneous emission rate depends strongly on sub-nm changes in gap size (FIG.3b,c). Such large enhancements enable quantum dots with initial lifetime of ~10 ns to emit photons on ultrafast timescales of 10 ps[59].

So far, we considered the weak coupling regime. However for emitters with large oscillator strengths embedded in plasmonic cavities, the strong coupling regime can be observed. This occurs because γ_r is now faster than plasmon decay, leading to reversible energy exchange between the emitter and cavity mode and the emergence of hybridized light-matter states. This can be realized for ensembles of many emitters such as molecular aggregates situated between gold disk dimers[74]. Recently, strong coupling was observed even at the single-emitter level by precisely orienting a single molecule in the 0.9 nm gap between a gold sphere and film using the guest-host chemistry of CB:dye described above. When the transition dipole moment of the molecule is favourably oriented with the gap plasmon, the scattering spectra split, indicating strong coupling (FIG.3d). With the molecule oriented perpendicular to the gap plasmon mode, no such splitting is observed emphasizing the need for precise control of emitter placement.

Plasmon-phonon vibrational coupling and optomechanics in nanogaps

A significant application for nanocavity plasmonics is the chemical interrogation of small numbers of molecules or ultrathin materials in real time, since the extreme field enhancements boost surface-enhanced Raman signals (SERS, scaling as E^4) of the samples located in the gap, enabling localized detection and fingerprinting. Early work on SERS blinking which was used to evidence single molecule signatures is likely enabled by plasmons trapped in crevices between nanoparticles[75–77]. Many nanostructures supporting nanocavity plasmons give such characteristic SERS, however in most cases the signals are irreproducible from individual structure to structure, limiting their utility. Key requirements are to precisely define the optical field distributions, enhancements, and orientations, as well as the capability to tether the molecules/layers of interest in specific positions and orientations. With suitable scaffolding, gap plasmons offer this capability, given the understanding of the modes above.

Robust SERS signatures are obtained when the gap is precisely defined by crystalline inorganics (such as CdTe few-unit-cell platelets[78]) or self-assembled monolayers (SAMs) of short alkyl chain or aromatic thiols. In the case of biphenyl-4-thiol (BPT) spacers creating NPoMs with d=1.3±0.1nm, the SERS spectra vary little with time or between different NPoMs (FIG.4a) and match well to density-functional theory (DFT) calculations. Such non-resonant molecules have no electronic resonances at the plasmon frequency, hence only virtual states are involved in the excitation of vibrations and molecular damage minimised. Typical SERS emission of 1000 counts s^{-1} mW^{-1} for each vibrational line ν correspond well to Raman cross sections $R_k \sim 0.5\ \mathrm{nm}^4/\mathrm{amu}$ (from DFT) and the vibrational mode coupling strength to plasmon mode ω_{mn} of

$$g_0 = \sqrt{\frac{\hbar R_k}{8\nu}}\,\frac{\omega_{mn}}{\varepsilon_g V_{\mathrm{W}}} \tag{8}$$

This gives total coupling $g = g_0\sqrt{N_m}$ for $N_m \sim$ 100 molecules inside the gap plasmon mode volume, assuming that all the molecules experience the same coupling. Small nanocavities thus enhance the SERS, while the plasmon coupling is to a collective vibration within all the molecules or bonds in an inorganic spacer layer. Variations in SERS amplitude in different nanogaps typically arise from inhomogeneity of the patch/NP sizes and (facet) shapes[47].

For a uniform Raman-active layer in the gap, assuming both incoming and outgoing light remains on resonance, the SERS amplitude is thus predicted to scale as $S \propto V_W E_{max}^4 \propto R^4/d^3$. When the resonance condition is not maintained a weaker dependence is observed experimentally, $S \propto R^3$, related to the scaling of facetting with R.[47]

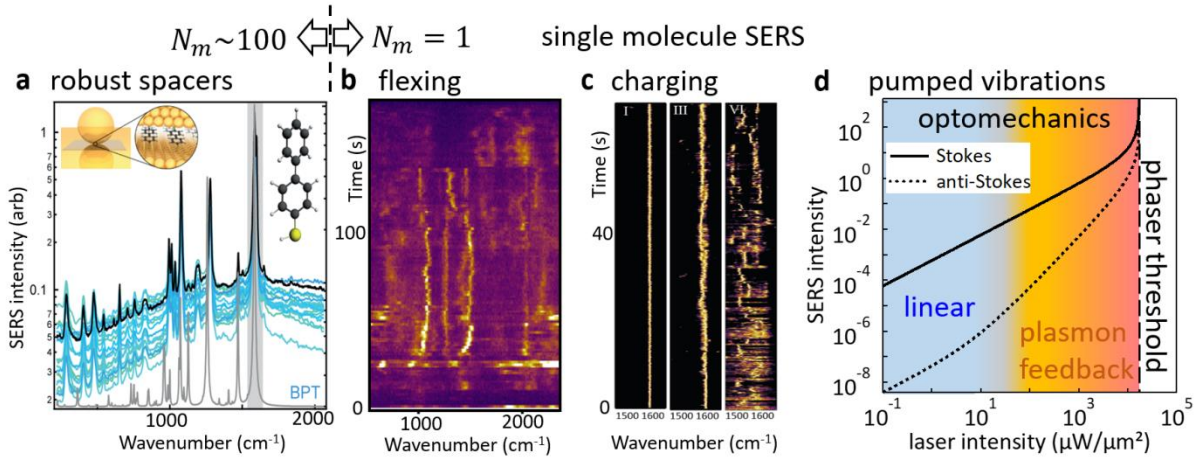

Figure 4 | Nanogap vibrational spectroscopy for chemistry and molecular optomechanics. a | Robust nanogaps with <100 molecules in a uniform molecular layer in the gap show strong reliable SERS spectra (shown here for 50 NPoMs). **b** | Single-molecule vibrational modes of lipids in the gap show spectral wandering of SERS in time due to their flexing. **c** | Redox of single methyl-viologen molecules gives jumps in the vibrational frequencies seen in the SERS spectra with time, as charges jump on and off the molecule. **d** | Molecular optomechanics regime induces non-linear enhancements of first anti-Stokes (dashed) and then Stokes (solid line) with pump power.

For molecular spacers which are either looser-packed or incorporate solvated ions, transient but extremely strong SERS signals can be seen[79]. These can now be understood to arise from the picocavities (see above) which provide sub-nm light confinement so that only single-molecule emission dominates over the rest of the molecules in the gap (the E_{pico}^4 SERS scaling gives additional hundredfold enhancement). How the single Au atom-molecular interaction forces lead to and stabilise this single molecule SERS is not yet fully understood.

Picocavities enable observation of single-molecule SERS signatures that evolve on ms-s timescales. For example, flexing of individual lipid molecules gives rise to continuous vibrational shifts to higher and lower energies of different bonds[80] (FIG.4b), which are correlated according to how far the bonds are from the flexing location[81]. By contrast, when redox-active molecules are incorporated in the gap, their charging digitally shifts their vibrational energies (FIG.4c) enabling single-molecule chemistry to be observed[82]. Reliable observations in such constructs open up opportunities for understanding and controlling chemistry at the single-molecule level.

An additional feature in nanogaps is the connection between the coupling of molecular vibrations to light and the opto-mechanical Hamiltonian, which are isomorphic[31,83]. Since the coupling g > 10meV in picocavities (due to sub-nm^3 volumes in eqn. 8), optomechanical effects can deliver considerable impacts on the Raman emission even in ambient conditions. Molecular optomechanics is able to provide stronger and nonlinear Raman emission as well as shaking molecules intensely enough to break chemical bonds[31,84]. We note that TERS also appears to often operate in this picocavity regime[19], implying new optomechanical

investigations can be accessed, as well as accounting for many of the fleeting signals previously seen (though long TERS integration times tend to aggregate these effects).

Conduction and bridging in nanogaps

So far we considered non-conducting spacers, however conductivity can also be controlled in such small gaps with promising applications in optical or electro-optic switching. The small nanocavity optical volumes (<10nm^3) imply minimal energy requirements for switching, reaching potentially <1zJ when few molecules are involved.

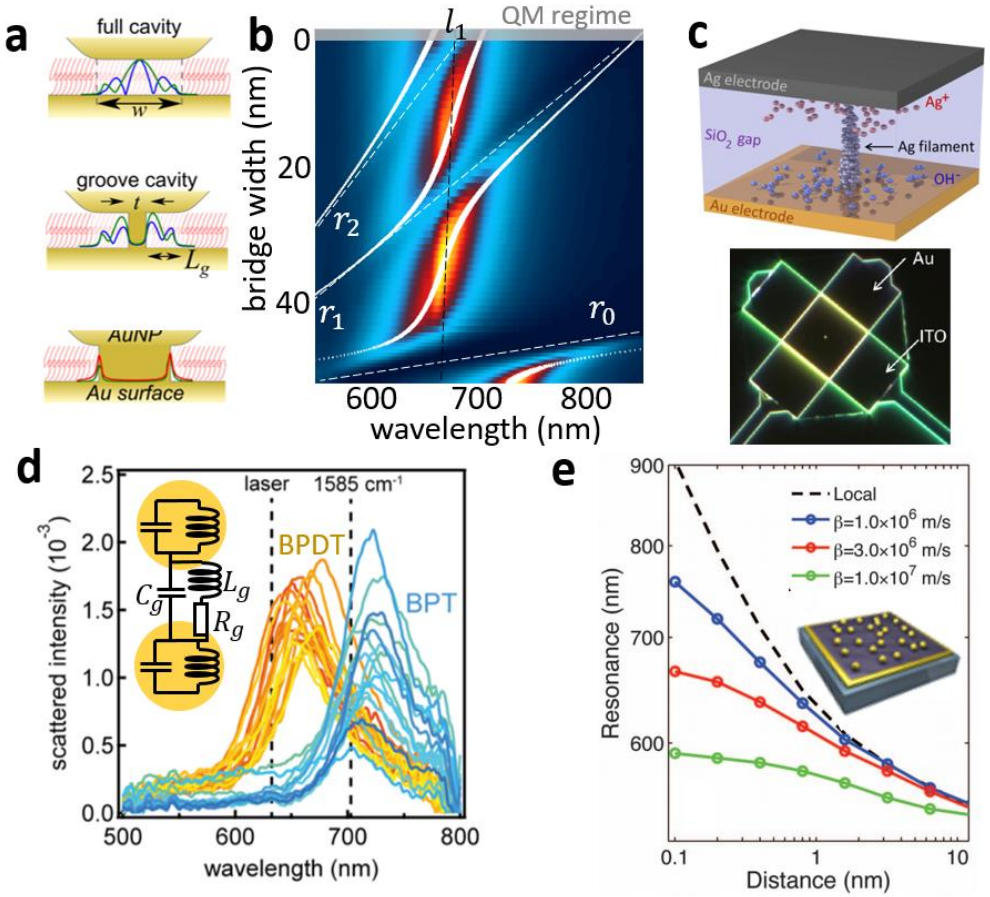

Figure 5 | Tuning nanocavities with conductivity. a | Effect of bridging across the nanogap for increasing bridge width (downwards) is to **b** | shift and mix modes in the scattering spectra (80nm NPoM, colours show simulated scattering, white dashed lines show groove modes r from model in main text). **c** | Resistive-RAM memory devices where applied voltage induces a stable nanowire exhibit gap tuning. **d** | Molecular layers show conduction-induced blue-shifts in the NPoM scattering resonance for different molecules (here BPDT has lower resistance than BPT). **e** | Modification of coupled resonance when including increasing quantum and non-local effects (through the hydrodynamic factor β).

Modelling facetted NPoMs including conducting bridges of increasing width spanning the gap shows abrupt tuning and reconfiguration of the nanogap modes[85] (FIG.5a,b). Extending the above Fabry-Perot MIM model explains this, assuming a perturbed cavity length $L_g = (w - t)/2$ is defined by facet/patch diameter w and bridge diameter t. Resonant 'groove' modes of this perturbed cavity are obtained at the resonance conditions $L_g = r' \cdot \lambda_r/2$. Here $r' = r + \varphi_g/2\pi$, where $r = 0,1,2,\ldots$ is the groove cavity mode order and $\varphi_g \sim \pi/2$ is a phase factor accounting for the boundary conditions of the nanocavity (now bounded by

the Au bridge opposite the open edge of the facet, FIG.5a). The energy of these groove modes is derived by solving the MIM dispersion (Eq.1) with groove wavevector $k_r = 2\pi/\lambda_r$, giving tuning of the modes (FIG.5b, white dashed lines).

As previously discussed, strongly-confined gap modes do not radiate directly, but only if they can mix with antenna modes. For an antenna mode λ_1^l at a wavelength of 700nm (vertical dashed line, FIG.5b) which is barely perturbed by the bridging, spectral positions of the hybrid modes are obtained from the eigenvalues of the coupled system (white lines). Fitting suitable coupling strengths reproduces the full simulations (colour map), with near-field distributions that evanescently decay within the bridge (FIG.5a) as predicted in this simple model. Such anti-crossings are directly seen in NPoM experiments using molecular layer gap spacers which are soft enough that optical irradiation can drive metallic nanowires between the two metal walls[85].

The modes blue-shift with thicker bridges because the groove cavity length L_g reduces, ejecting modes one by one from the gap[85]. The blue-shifts and mode-crossings thus allow conducting bridge diameters and locations to be determined. The model shows field enhancement in the gap is typically three times smaller in the crevice after the gap has closed, thus giving 1-2 orders of magnitude smaller SERS from shorted gaps.

Such nanowire bridging is technologically important because it forms the basis of one class of memristive or resistive-random-access-memory (RRAM) devices, under intense investigation. These form two-terminal non-volatile low-energy storage cells, in which an applied threshold voltage is sufficient to drive a conductive link from one contact to another, that can be disassembled with sufficient reverse voltage. A major issue in these RRAMs is their sporadic failure after >10^5 cycles, from unknown causes that are hard to image in electron microscopy. By integrating such devices as a patch antenna MIM (FIG.5c), dark-field spectroscopy is capable of watching the real-time dynamics of the nanowire through their groove modes[86]. Further studies have utilised a waveguide configuration[87], while DFT simulations confirm that such bridges can form through single-atom nanowires[56]. Optical characterization in such nanogaps offers a number of advantages over electron microscopy including access to in-situ non-destructive dynamics under ambient operation conditions, revealing contact morphologies on the nanometre scale.

Even without metallic bridges, conductive spacers influence the MIM modes[88]. Using SAMs of identical thickness (calibrated using ellipsometry) but differing in their electronic transport (through only a single additional sulphur atom on each molecule which turns on hybridisation with the Au) gives 60nm blue-shifts of the NPoM coupled plasmon (FIG.5d). In this case, instead of groove modes the imaginary contribution to the vertical gap polarizability is increased, which partly discharges the nanogap capacitor within each optical half-cycle. The LCR model accounts for this when the gap capacitance is shunted by gap resistance R_g and kinetic inductance L_g (FIG.5d, inset). The blue-shifted screened antenna mode wavelength is then given (in the limit of conductivities greater than the quantum conductance $G_0 = (13k\Omega)^{-1}$ by[46]

$$\lambda_{\text{screened}}^{l=1} = \lambda_1^l/(1 + 4\varepsilon_d\omega_L^2/\omega_p^2) \quad (9)$$

with the inductive coupling $\omega_L = 1/\sqrt{L_g C_s}$ for plasma frequency $\omega_p = 2\pi c/\lambda_p$ and unscreened antenna mode λ_1^l from Eqn.(5). This arises from a self-inductance of nanowires

forming the effective conductive channel, since moving electrons have to drag their magnetic field lines with them, increasing their inertia. At optical frequencies, current only travels in a nm-thick outer sheath (depth Λ compared to nanowire radius a) yielding $L_g \sim f/(a\varepsilon_0\omega_p^2)$ where fill fraction $f = \pi^{-1}(1 + d/2\Lambda)$. Substituting this gives wavelength shifts from the conductive layer in small gaps of[46]

$$\lambda_{\text{screened}}^{l=1} = \lambda_1^l \left(1 - \varepsilon_d \frac{a}{R}\right) \tag{10}$$

which blue-shifts linearly with increasing width of the conducting linker, as confirmed by detailed simulations[88].

Another prominent effect arising from creating conductive channels across plasmonic gaps is the emergence of low energy modes for sufficiently large values of conductance. These modes are associated with charge transfer across the gap which completely screens capacitive gap modes, producing plasmonic oscillations that extend over the entire particle-substrate system. The conductance threshold G_{CTP} for such charge-transfer plasmons to appear at long wavelengths λ_{CTP} is given by[88]

$$G_{\text{CTP}} = \frac{c}{2\lambda_{\text{CTP}}} \frac{R^2}{d}$$

which is larger than that needed for the initial screening of the gap plasmons derived in Eqn.(10). The emergence of these charge transfer plasmons has been identified in several experiments involving nanogaps in metallic dimers[89], nanoshells[90], and particle chains[91–93].

When the gap is deeply sub-nm (d<0.5nm) quantum corrections become important, covered in a recent review[94]. In brief, two corrections can be understood from (a) the effect at optical frequencies of the relative position of the centroid of charge density of the electronic excited state (surface plasmon) at the surface of the Au[95] (beyond the classical localization at the sharp boundary due to the wavefunctions of the confined states), and (b) the quantum tunnelling through the dielectric gap which produces a shunt resistance R_g with effect similar to that noted above. Both these reduce the charge stored at the metallic gap surfaces, thus blue-shifting the gap plasmon[52] (FIG.5e). Experimentally stabilising such sub-nm gaps is difficult, with experiments using conducting nanotips[52], molecular spacers[18,94,96], or graphene monolayers[28], among others.

Applications and new directions

Several techniques now produce well-controlled nm-spacers over large areas, both by top-down (such as atomic layer) deposition or bottom-up coatings such as SAMs. This opens up the capability to create 'metasurfaces' with tailored electric and magnetic response. Even disordered arrays accessible by bottom-up deposition can create >cm-scale surfaces covered by particle-on-a-mirror structures (FIG.6a). By optimizing the mean distance between the plasmonic elements and the gap size, the response of the surface can be impedance matched to free space resulting in near-perfect absorption at the plasmon resonance wavelength[97–99]. Strongly enhanced absorption of light at particular frequencies over large areas is useful for hot-electron photodetectors[100], non-bandgap-limited thermal detectors[101], light harvesting, surface coatings and enhanced non-linear generation, among other possibilities.

Periodically tiling these gap elements mixes in a sharper lattice-mode response[102]. Fabricating these currently demands lithographic lateral patterning such as photolithography[103], but enables pixels to be created comprised of metasurfaces with different resonances (FIG.6a). This enables simultaneous on-chip capture of spectral and spatial information for multi- or hyper-spectral imaging with the potential to span ultraviolet to infrared spectral regions using a single material platform, since absorption arises from 'structural-colour' rather than depending on a material bandgap. Hybrid bottom-up and top-down fabrication approaches can also realize combinatorial plasmonic-colour printing where the intensity of each RGB-channel is controlled by varying the fill-fraction or shape of nanoparticles on the surfaces[103,104]. This could find use for fade-free printing, friend or foe IR images or ultra-high resolution printing. Key challenges to resolve are creating large-area films at low cost which may preclude conventional or even imprint lithographies. Perhaps most promising are self-assembly approaches requiring nanoscale design but which are tolerant enough to variable gap and particle sizes. More difficult is the associated backplane electronic control which has not yet been shown to be low energy or scalable enough. Other opportunities in this area include improved nanoscale designs which give stronger contrast and faster (FIG.6a, τ) and better colour tuning (λ).

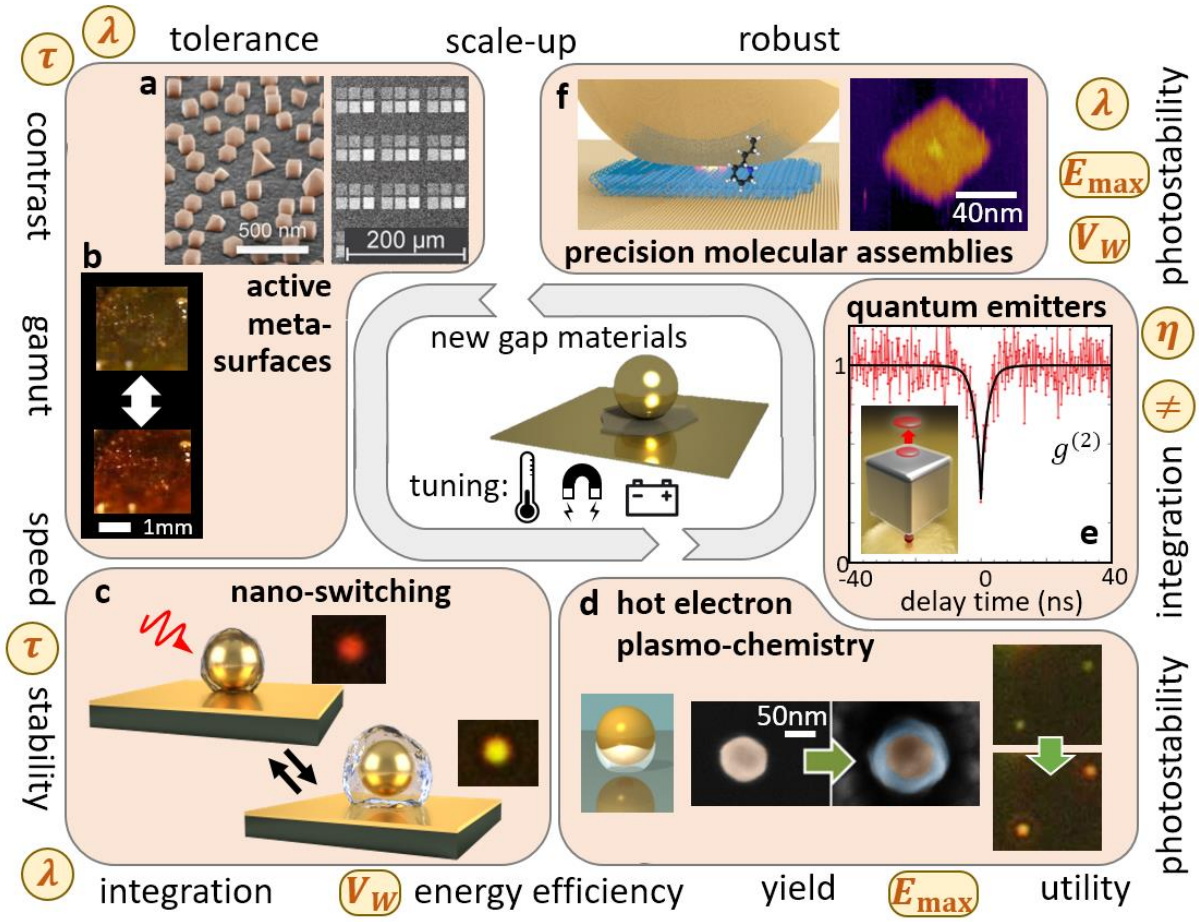

Figure 6 | Exploitation of nanocavities for new devices: molecular spintronics, thermo-optics, electro-optics. **a,b** | Colour-changing metasurfaces and wallpapers: tuning thin-film scattered colours. **c** | Low-energy optical switching of single NPoM. **d** | Hot electron plasmo-chemistry dynamically grows polymer coatings. **e** | Room temperature quantum emitters. **f** | Precision

molecular assembly: tuning molecular interactions, coherence and forces. Key demands for these applications around the outside, together with figures of merit (circled in yellow).

Due to the high local field enhancements in the gap, a small change in the properties of the material in this region, such as index of refraction or thickness, results in a large change in plasmon resonance, useful for real-time reconfigurable structures[105–107] or sensing[108]. In this way large area sub-µs colour changing wallpapers[109] (FIG.6b) or individual optically-triggered NPoM switching (FIG.6c) deliver low energy actuation and access novel nano-opto-mechanical devices[110]. The search for electrical tuning has recently intensified with electrical gating configurations utilised[111,112]. The sensitivity of the plasmon modes to conductivity[113] points to a new field of molecular opto-electronics, with particular interest for spin-gated and switchable molecular devices. To progress this area, switchable gap materials have to be shown to be fast (τ<1ns is feasible due to the small volumes V_W), robust over thousands of cycles, as well as deliver low energy performance. Integration into optical backplanes or fibre geometries is a key goal requiring suitable materials combination.

Extreme nanooptics enables chemical reactions at the molecular scale to be studied and influenced, alongside functional surface (electro)-chemistry. Similarly dynamic bio-sensing is envisaged, for instance of individual protein-complex machineries. Nanogap assemblies are being exploited to create the 'intelligent toilet', capable of routine low-cost personalised healthcare[114]. The nanogap geometry is also particularly suited for study of electrochemical processes in the direct vicinity of electrodes, by tracking dynamically both SERS and scattering during reactions[115,116]. This application space has been plagued by the difficulty of translating research excitement into market traction, as specific applications have not been sufficiently targeted for large-scale trials. Part of the problem is collecting enough data to prove medical utility, and issues such as reproducibility of plasmonic nanoparticle surfactant chemistries, shelf life, contaminants, and consistency of quantitative performance are still to be understood in sufficient detail.

Plasmonic nanostructures are capable of emitting 'hot electrons' under irradiation[117]. Several recent experiments in nanogaps show these effects directly, via chemical reactions under TERS tips[118,119], reversible redox of single molecules in NPoMs[82], and free radical polymerisation of monomers to coat inside nanogaps[120] (FIG.6d). The tunability of plasmon modes and electronics states opens enormous opportunities in studying chemistry at the nanoscale in these systems, with many unanswered questions about the nature of molecule-surface interactions, and the efficiency of hot-electron plasmo-chemistry[117]. While this area is promising, quantitative information is lacking and unsubstantiated claims abound. Most crucial is to explore a wider range of industrially-relevant reactions, and compare against state-of-the-art-processes, including the full energy and materials sourcing costs. The fraction of hot electrons per incident photon (which depends on the field enhancement $E_{\max}$), and their energy spread must be measured, requiring development of new experimental techniques.

When emitters are embedded in nanogaps, as discussed above, their spontaneous emission rate can be sped up significantly. This can enable a host of ultrafast optoelectronic applications, potentially in the THz-regime, from modulators to ultrafast LEDs and photodetectors for on-chip information processing or even free-space optical

communications[121]. This also broadens the range of luminescent materials of interest for practical applications since the intrinsic material properties become less important. New questions then emerge as to material stability and properties under extreme field enhancements and high pumping conditions. Applications for on-chip quantum information processing could also be imagined as ultrafast single photon sources have been demonstrated using quantum dots in nanogaps[60] (FIG.6e), while spin-selectivity demonstrated for nitrogen-vacancy centers in diamond[122] and enhanced spontaneous parametric downconversion[123] may enable the creation of entangled-photon pairs from ultrathin layers of nonlinear material. Room temperature quantum emitters of high efficiency η capable of being packaged and used (at least in research facilities) requires key advances in developing photostable molecules (or other constructs), as well as improved tunability to make indistinguishable sources ('$\neq$'). Solid-state emitters such as rare earth ions in ultrathin films may prove a valuable route to integrate with these plasmonic nanocavities.

Advances in deterministic nano-assembly using DNA origami now allow specific numbers and types of molecules to be precisely inserted within $\pm$1nm locations inside the gap[65] (FIG.6f). In this arena, material science and molecular science merge into precision nanotechnology. This allows new investigations of the plasmonic-modified intermolecular interactions including their electronic and vibrational coherences. In addition the large field gradients can induce 'picoforces' capable of bending and moving molecules. This area is extremely promising, and a wide array of different constructs can be conceived which open up fundamental fields, however applications require much more photostable constructs, possibly using biomimetic redox strategies to avoid photobleaching steps.

With extreme optical confinement comes the capability to observe the motion of single metal atoms, which is induced by optical irradiation of the gap modes[31]. This explains many observations in plasmonics over the years, such as the slow degradation of SERS properties at room temperature (caused by thermal excitation over the $\sim$0.8eV barrier for adatom site hopping). Irradiation moves gold or silver atoms[85], however its mechanism is not yet well understood, with both optical gradient forces at the single atom level ('picotweezers'), and non-equilibrium thermal gradients plausible candidates. Controllable single-atom optical switches are thus an exciting prospect for this extreme nano-optics.

Acknowledgment: We acknowledge support from UK EPSRC grants EP/G060649/1, EP/L027151/1, EP/G037221/1, EPSRC NanoDTC, ERC grant LINASS 320503, and FIS2016-80174-P from Spanish Ministry MINECO. M.H.M. acknowledges support from the Air Force Office of Scientific Research (AFOSR, Grant. No. FA9550-15-1-0301) and the National Science Foundation (DMR-1454523). We appreciate extensive data and discussions on the mode scaling with Angela Demetriadou, and enormous contributions from many members of our research groups over the past decade.

Author contributions: All authors contributed equally to the preparation of this manuscript.

Data availability

All relevant data present in this publication can be accessed at: https://www.repository.cam.ac.uk/handle/XXXX/XXXXXX

Competing financial interests:
The authors declare no competing financial interests.

References:

1. Ritchie, R. H. Plasma Losses by Fast Electrons in Thin Films. *Phys. Rev.* **106,** 874–881 (1957).
2. Krenn, J. R. *et al.* Squeezing the Optical Near-Field Zone by Plasmon Coupling of Metallic Nanoparticles. *Phys. Rev. Lett.* **82,** 2590–2593 (1999).
3. Krenn, J. R. *et al.* Direct observation of localized surface plasmon coupling. *Phys. Rev. B* **60,** 5029–5033 (1999).
4. Ditlbacher, H., Krenn, J. R., Schider, G., Leitner, A. & Aussenegg, F. R. Two-dimensional optics with surface plasmon polaritons. *Appl. Phys. Lett.* **81,** 1762–1764 (2002).
5. Maier, S. A. *et al.* Local detection of electromagnetic energy transport below the diffraction limit in metal nanoparticle plasmon waveguides. *Nat. Mater.* **2,** 229–232 (2003).
6. Gramotnev, D. K. & Bozhevolnyi, S. I. Plasmonics beyond the diffraction limit. *Nat. Photonics* **4,** 83–91 (2010).
7. Yang, W., Schatz, G. C. & Van Duyne, R. P. Discrete dipole approximation for calculating extinction and Raman intensities for small particles with arbitrary shapes. *J. Chem. Phys.* **103,** 869–875 (1995).
8. Kottmann, J. P., Martin, O. J. F., Smith, D. R. & Schultz, S. Spectral response of plasmon resonant nanoparticles with a non-regular shape. *Opt. Express* **6,** 213 (2000).
9. Mock, J. J., Barbic, M., Smith, D. R., Schultz, D. A. & Schultz, S. Shape effects in plasmon resonance of individual colloidal silver nanoparticles. *J. Chem. Phys.* **116,** 6755–6759 (2002).
10. Kelly, K. L., Coronado, E., Zhao, L. L. & Schatz, G. C. The Optical Properties of Metal Nanoparticles: The Influence of Size, Shape, and Dielectric Environment. *J. Phys. Chem. B* **107,** 668–677 (2003).
11. Xu, H., Bjerneld, E. J., Käll, M. & Börjesson, L. Spectroscopy of Single Hemoglobin Molecules by Surface Enhanced Raman Scattering. *Phys. Rev. Lett.* **83,** 4357–4360 (1999).
12. Kottmann, J. P. & Martin, O. J. F. Plasmon resonant coupling in metallic nanowires. *Opt. Express* **8,** 655 (2001).
13. Hao, E. & Schatz, G. C. Electromagnetic fields around silver nanoparticles and dimers. *J. Chem. Phys.* **120,** 357–366 (2004).
14. Ghosh, S. K. & Pal, T. Interparticle Coupling Effect on the Surface Plasmon Resonance of Gold Nanoparticles: From Theory to Applications. *Chem. Rev.* **107,** 4797–4862 (2007).
15. Koh, A. L., Fernández-Domínguez, A. I., McComb, D. W., Maier, S. A. & Yang, J. K. W. High-Resolution Mapping of Electron-Beam-Excited Plasmon Modes in Lithographically Defined Gold Nanostructures. *Nano Lett.* **11,** 1323–1330 (2011).
16. Lévêque, G. & Martin, O. J. F. Optical interactions in a plasmonic particle coupled to a metallic film. *Opt. Express* **14,** 9971 (2006).
17. Nordlander, P. & Le, F. Plasmonic structure and electromagnetic field enhancements in the metallic nanoparticle-film system. *Appl. Phys. B* **84,** 35–41 (2006).
18. Kern, J. *et al.* Atomic-Scale Confinement of Resonant Optical Fields. *Nano Lett.* **12,** 5504–5509 (2012).
19. Zhang, R. *et al.* Chemical mapping of a single molecule by plasmon-enhanced Raman scattering. *Nature* **498,** 82–86 (2013).
20. Zhang, R. *et al.* Chemical mapping of a single molecule by plasmon-enhanced Raman scattering. *Nature* **498,** 82–86 (2013).
21. Zhang, Y. *et al.* Sub-nanometre control of the coherent interaction between a single molecule and a plasmonic nanocavity. *Nat. Commun.* **8,** 15225 (2017).
22. Dathe, A., Ziegler, M., Hübner, U., Fritzsche, W. & Stranik, O. Electrically Excited Plasmonic Nanoruler for Biomolecule Detection. *Nano Lett.* **16,** 5728–5736 (2016).
23. Tuniz, A. & Schmidt, M. A. Interfacing optical fibers with plasmonic nanoconcentrators. *Nanophotonics* **7,** 1279–1298 (2018).
24. Kuttge, M., García de Abajo, F. J. & Polman, A. Ultrasmall Mode Volume Plasmonic Nanodisk Resonators. *Nano Lett.* **10,** 1537–1541 (2010).

25. Hu, M., Ghoshal, A., Marquez, M. & Kik, P. G. Single Particle Spectroscopy Study of Metal-Film-Induced Tuning of Silver Nanoparticle Plasmon Resonances. *J. Phys. Chem. C* **114,** 7509–7514 (2010).
26. Mock, J. J. *et al.* Distance-Dependent Plasmon Resonant Coupling between a Gold Nanoparticle and Gold Film. *Nano Lett.* **8,** 2245–2252 (2008).
27. Ciraci, C. *et al.* Probing the Ultimate Limits of Plasmonic Enhancement. *Science (80-.).* **337,** 1072–1074 (2012).
28. Mertens, J. *et al.* Controlling subnanometer gaps in plasmonic dimers using graphene. *Nano Lett.* **13,** 5033–5038 (2013).
29. Shvets, G. Photonic approach to making a material with a negative index of refraction. *Phys. Rev. B* **67,** 035109 (2003).
30. Dionne, J. A., Sweatlock, L. A., Atwater, H. A. & Polman, A. Plasmon slot waveguides: Towards chip-scale propagation with subwavelength-scale localization. *Phys. Rev. B* **73,** 035407 (2006).
31. Benz, F. *et al.* Single-molecule optomechanics in "picocavities". *Science (80-.).* **354,** 726–729 (2016).
32. K. F. Lee. *Principles of antenna theory*. (John Wiley & Sons, Ltd, 1984).
33. Parzefall, M. *et al.* Antenna-coupled photon emission from hexagonal boron nitride tunnel junctions. *Nat. Nanotechnol.* **10,** 1058–1063 (2015).
34. Du, W., Wang, T., Chu, H.-S. & Nijhuis, C. A. Highly efficient on-chip direct electronic–plasmonic transducers. *Nat. Photonics* **11,** 623–627 (2017).
35. Bozhevolnyi, S. I. & Søndergaard, T. General properties of slow-plasmon resonant nanostructures: nano-antennas and resonators. *Opt. Express* **15,** 10869 (2007).
36. Zayats, A. V., Smolyaninov, I. I. & Maradudin, A. A. Nano-optics of surface plasmon polaritons. *Phys. Rep.* **408,** 131–314 (2005).
37. Bozhevolnyi, S. I. & Søndergaard, T. General properties of slow-plasmon resonant nanostructures: nano-antennas and resonators. *Opt. Express* **15,** 10869 (2007).
38. Kuttge, M., Cai, W., García de Abajo, F. J. & Polman, A. Dispersion of metal-insulator-metal plasmon polaritons probed by cathodoluminescence imaging spectroscopy. *Phys. Rev. B* **80,** 033409 (2009).
39. Sigle, D. O. *et al.* Monitoring Morphological Changes in 2D Monolayer Semiconductors Using Atom-Thick Plasmonic Nanocavities. *ACS Nano* **9,** 825–830 (2015).
40. Alcaraz Iranzo, D. *et al.* Probing the ultimate plasmon confinement limits with a van der Waals heterostructure. *Science (80-.).* **360,** 291–295 (2018).
41. Tserkezis, C. *et al.* Hybridization of plasmonic antenna and cavity modes: Extreme optics of nanoparticle-on-mirror nanogaps. *Phys. Rev. A* **92,** 053811 (2015).
42. Kleemann, M.-E. *et al.* Revealing Nanostructures through Plasmon Polarimetry. *ACS Nano* **11,** 850–855 (2017).
43. Engheta, N., Salandrino, A. & Alù, A. Circuit Elements at Optical Frequencies: Nanoinductors, Nanocapacitors, and Nanoresistors. *Phys. Rev. Lett.* **95,** 095504 (2005).
44. Liu, N. *et al.* Individual Nanoantennas Loaded with Three-Dimensional Optical Nanocircuits. *Nano Lett.* **13,** 142–147 (2013).
45. Greffet, J.-J., Laroche, M. & Marquier, F. Impedance of a Nanoantenna and a Single Quantum Emitter. *Phys. Rev. Lett.* **105,** 117701 (2010).
46. Benz, F. *et al.* Generalized circuit model for coupled plasmonic systems. *Opt. Express* **23,** 33255 (2015).
47. Benz, F. *et al.* SERS of Individual Nanoparticles on a Mirror: Size Does Matter, but so Does Shape. *J. Phys. Chem. Lett.* **7,** 2264–2269 (2016).
48. Bowen, P. T. & Smith, D. R. Coupled-mode theory for film-coupled plasmonic nanocubes. *Phys. Rev. B* **90,** 195402 (2014).
49. Esteban, R. *et al.* The Morphology of Narrow Gaps Modifies the Plasmonic Response. *ACS Photonics* **2,** 295–305 (2015).
50. Li, R.-Q., Hernángomez-Pérez, D., García-Vidal, F. J. & Fernández-Domínguez, A. I. Transformation Optics Approach to Plasmon-Exciton Strong Coupling in Nanocavities. *Phys. Rev. Lett.* **117,** 107401 (2016).
51. Chikkaraddy, R. *et al.* How Ultranarrow Gap Symmetries Control Plasmonic Nanocavity Modes: From Cubes to Spheres in the Nanoparticle-on-Mirror. *ACS Photonics* **4,** 469–475 (2017).
52. Savage, K. J. *et al.* Revealing the quantum regime in tunnelling plasmonics. *Nature* **491,** 574–577 (2012).
53. Sauvan, C., Hugonin, J. P., Maksymov, I. S. & Lalanne, P. Theory of the Spontaneous Optical Emission of Nanosize Photonic and Plasmon Resonators. *Phys. Rev. Lett.* **110,** 237401 (2013).
54. Sanders, A. *et al.* Understanding the plasmonics of nanostructured atomic force microscopy tips. *Appl.*

Phys. Lett. **109,** 109–112 (2016).
55. Ropers, C. *et al.* Grating-Coupling of Surface Plasmons onto Metallic Tips: A Nanoconfined Light Source. *Nano Lett.* **7,** 2784–2788 (2007).
56. Marchesin, F., Koval, P., Barbry, M., Aizpurua, J. & Sánchez-Portal, D. Plasmonic Response of Metallic Nanojunctions Driven by Single Atom Motion: Quantum Transport Revealed in Optics. *ACS Photonics* **3,** 269–277 (2016).
57. Barbry, M. *et al.* Atomistic Near-Field Nanoplasmonics: Reaching Atomic-Scale Resolution in Nanooptics. *Nano Lett.* **15,** 3410–3419 (2015).
58. Urbieta, M. *et al.* Atomic-Scale Lightning Rod Effect in Plasmonic Picocavities: A Classical View to a Quantum Effect. *ACS Nano* **12,** 585–595 (2018).
59. Hoang, T. B. *et al.* Ultrafast spontaneous emission source using plasmonic nanoantennas. *Nat. Commun.* **6,** (2015).
60. Hoang, T. B., Akselrod, G. M. & Mikkelsen, M. H. Ultrafast Room-Temperature Single Photon Emission from Quantum Dots Coupled to Plasmonic Nanocavities. *Nano Lett.* **16,** (2016).
61. Akselrod, G. M. *et al.* Leveraging nanocavity harmonics for control of optical processes in 2d semiconductors. *Nano Lett.* **15,** (2015).
62. Huang, J., Akselrod, G. M., Ming, T., Kong, J. & Mikkelsen, M. H. Tailored Emission Spectrum of 2D Semiconductors Using Plasmonic Nanocavities. *ACS Photonics* **5,** (2018).
63. Rose, A. *et al.* Control of radiative processes using tunable plasmonic nanopatch antennas. *Nano Lett.* **14,** (2014).
64. Akselrod, G. M. *et al.* Probing the mechanisms of large Purcell enhancement in plasmonic nanoantennas. *Nat. Photonics* **8,** (2014).
65. Chikkaraddy, R. *et al.* Mapping Nanoscale Hotspots with Single-Molecule Emitters Assembled into Plasmonic Nanocavities Using DNA Origami. *Nano Lett.* **18,** 405–411 (2018).
66. Chikkaraddy, R. *et al.* Single-molecule strong coupling at room temperature in plasmonic nanocavities. *Nature* **535,** 127–130 (2016).
67. Kinkhabwala, A. *et al.* Large single-molecule fluorescence enhancements produced by a bowtie nanoantenna. *Nat. Photonics* **3,** 654–657 (2009).
68. Akselrod, G. M. *et al.* Efficient Nanosecond Photoluminescence from Infrared PbS Quantum Dots Coupled to Plasmonic Nanoantennas. *ACS Photonics* **3,** (2016).
69. Argyropoulos, C., Ciracì, C. & Smith, D. R. Enhanced optical bistability with film-coupled plasmonic nanocubes. *Appl. Phys. Lett.* **104,** 63108 (2014).
70. Kongsuwan, N. *et al.* Suppressed Quenching and Strong-Coupling of Purcell-Enhanced Single-Molecule Emission in Plasmonic Nanocavities. *ACS Photonics* **5,** 186–191 (2018).
71. Anger, P., Bharadwaj, P. & Novotny, L. Enhancement and Quenching of Single-Molecule Fluorescence. *Phys. Rev. Lett.* **96,** 113002 (2006).
72. Pelton, M. Modified spontaneous emission in nanophotonic structures. *Nat. Photonics* **9,** 427–435 (2015).
73. Russell, K. J., Liu, T.-L., Cui, S. & Hu, E. L. Large spontaneous emission enhancement in plasmonic nanocavities. *Nat. Photonics* **6,** 459–462 (2012).
74. Schlather, A. E., Large, N., Urban, A. S., Nordlander, P. & Halas, N. J. Near-Field Mediated Plexcitonic Coupling and Giant Rabi Splitting in Individual Metallic Dimers. *Nano Lett.* **13,** 3281–3286 (2013).
75. Kneipp, K. *et al.* Single Molecule Detection Using Surface-Enhanced Raman Scattering (SERS). *Phys. Rev. Lett.* **78,** 1667–1670 (1997).
76. Nie, S. Probing Single Molecules and Single Nanoparticles by Surface-Enhanced Raman Scattering. *Science (80-.).* **275,** 1102–1106 (1997).
77. Qian, X.-M. & Nie, S. M. Single-molecule and single-nanoparticle SERS: from fundamental mechanisms to biomedical applications. *Chem. Soc. Rev.* **37,** 912 (2008).
78. Sigle, D. O., Hugall, J. T., Ithurria, S., Dubertret, B. & Baumberg, J. J. Probing Confined Phonon Modes in Individual CdSe Nanoplatelets Using Surface-Enhanced Raman Scattering. *Phys. Rev. Lett.* **113,** 087402 (2014).
79. Weiss, A. & Haran, G. Time-Dependent Single-Molecule Raman Scattering as a Probe of Surface Dynamics. *J. Phys. Chem. B* **105,** 12348–12354 (2001).
80. Taylor, R. W. *et al.* Watching individual molecules flex within lipid membranes using SERS. *Sci. Rep.* **4,** 5940 (2015).
81. Sonntag, M. D., Chulhai, D., Seideman, T., Jensen, L. & Van Duyne, R. P. The Origin of Relative Intensity Fluctuations in Single-Molecule Tip-Enhanced Raman Spectroscopy. *J. Am. Chem. Soc.* **135,** 17187–

17192 (2013).
82. De Nijs, B. *et al.* Plasmonic tunnel junctions for single-molecule redox chemistry. *Nat. Commun.* **8,** 1–7 (2017).
83. Schmidt, M. K., Esteban, R., Benz, F., Baumberg, J. J. & Aizpurua, J. Linking classical and molecular optomechanics descriptions of SERS. *Faraday Discuss.* **205,** 31–65 (2017).
84. Lombardi, A. *et al.* Pulsed Molecular Optomechanics in Plasmonic Nanocavities: From Nonlinear Vibrational Instabilities to Bond-Breaking. *Phys. Rev. X* **8,** 011016 (2018).
85. Mertens, J. *et al.* Tracking Optical Welding through Groove Modes in Plasmonic Nanocavities. *Nano Lett.* **16,** 5605–5611 (2016).
86. Di Martino, G., Tappertzhofen, S., Hofmann, S. & Baumberg, J. Nanoscale Plasmon-Enhanced Spectroscopy in Memristive Switches. *Small* **12,** 1334–1341 (2016).
87. Emboras, A. *et al.* Nanoscale Plasmonic Memristor with Optical Readout Functionality. *Nano Lett.* **13,** 6151–6155 (2013).
88. Pérez-González, O. *et al.* Optical Spectroscopy of Conductive Junctions in Plasmonic Cavities. *Nano Lett.* **10,** 3090–3095 (2010).
89. Scholl, J. A. *et al.* Evolution of Plasmonic Metamolecule Modes in the Quantum Tunneling Regime. *ACS Nano* **10,** 1346–1354 (2016).
90. Lin, L. *et al.* Nanooptics of Plasmonic Nanomatryoshkas: Shrinking the Size of a Core–Shell Junction to Subnanometer. *Nano Lett.* **15,** 6419–6428 (2015).
91. Fontana, J. & Ratna, B. R. Highly tunable gold nanorod dimer resonances mediated through conductive junctions. *Appl. Phys. Lett.* **105,** 011107 (2014).
92. Herrmann, L. O. *et al.* Threading plasmonic nanoparticle strings with light. *Nat. Commun.* **5,** (2014).
93. Koya, A. N. & Lin, J. Charge transfer plasmons: Recent theoretical and experimental developments. *Appl. Phys. Rev.* **4,** 021104 (2017).
94. Zhu, W. & Crozier, K. B. Quantum mechanical limit to plasmonic enhancement as observed by surface-enhanced Raman scattering. *Nat. Commun.* **5,** 5228 (2014).
95. Teperik, T. V., Nordlander, P., Aizpurua, J. & Borisov, A. G. Robust Subnanometric Plasmon Ruler by Rescaling of the Nonlocal Optical Response. *Phys. Rev. Lett.* **110,** 263901 (2013).
96. Zhu, W. *et al.* Quantum mechanical effects in plasmonic structures with subnanometre gaps. *Nat. Commun.* **7,** 11495 (2016).
97. Akselrod, G. M. *et al.* Large-Area Metasurface Perfect Absorbers from Visible to Near-Infrared. *Adv. Mater.* **27,** (2015).
98. Moreau, A. *et al.* Controlled-reflectance surfaces with film-coupled colloidal nanoantennas. *Nature* **492,** 86–89 (2012).
99. Rozin, M. J., Rosen, D. A., Dill, T. J. & Tao, A. R. Colloidal metasurfaces displaying near-ideal and tunable light absorbance in the infrared. *Nat. Commun.* **6,** 7325 (2015).
100. Brongersma, M. L., Halas, N. J. & Nordlander, P. Plasmon-induced hot carrier science and technology. *Nat. Nanotechnol.* **10,** 25–34 (2015).
101. Mauser, K. W. *et al.* Resonant thermoelectric nanophotonics. *Nat. Nanotechnol.* **12,** 770–775 (2017).
102. Bowen, P. T., Baron, A. & Smith, D. R. Effective-medium description of a metasurface composed of a periodic array of nanoantennas coupled to a metallic film. *Phys. Rev. A* **95,** 033822 (2017).
103. Stewart, J. W., Akselrod, G. M., Smith, D. R. & Mikkelsen, M. H. Toward Multispectral Imaging with Colloidal Metasurface Pixels. *Adv. Mater.* **29,** 1602971 (2017).
104. Goh, X. M. *et al.* Three-dimensional plasmonic stereoscopic prints in full colour. *Nat. Commun.* **5,** 5361 (2014).
105. Hoang, T. B. & Mikkelsen, M. H. Broad electrical tuning of plasmonic nanoantennas at visible frequencies. *Appl. Phys. Lett.* **108,** 183107 (2016).
106. Wilson, W. M., Stewart, J. W. & Mikkelsen, M. H. Surpassing Single Line Width Active Tuning with Photochromic Molecules Coupled to Plasmonic Nanoantennas. *Nano Lett.* **18,** (2018).
107. Ding, T., Mertens, J., Sigle, D. O. & Baumberg, J. J. Capillary-Force-Assisted Optical Tuning of Coupled Plasmons. *Adv. Mater.* **27,** 6457–6461 (2015).
108. Powell, A. W. *et al.* Plasmonic Gas Sensing Using Nanocube Patch Antennas. *Adv. Opt. Mater.* **4,** 634–642 (2016).
109. Ding, T. *et al.* Fast Dynamic Color Switching in Temperature-Responsive Plasmonic Films. *Adv. Opt. Mater.* **4,** 877–882 (2016).
110. Cormier, S., Ding, T., Turek, V. & Baumberg, J. J. Actuating Single Nano-Oscillators with Light. *Adv. Opt. Mater.* **6,** 1701281 (2018).

111. Holsteen, A. L., Raza, S., Fan, P., Kik, P. G. & Brongersma, M. L. Purcell effect for active tuning of light scattering from semiconductor optical antennas. *Science (80-.).* **358,** 1407–1410 (2017).
112. Liu, X. *et al.* Electrical tuning of a quantum plasmonic resonance. *Nat. Nanotechnol.* **12,** 866–870 (2017).
113. Benz, F. *et al.* Nanooptics of Molecular-Shunted Plasmonic Nanojunctions. *Nano Lett.* **15,** 669–674 (2015).
114. Kasera, S., Herrmann, L. O., Barrio, J. del, Baumberg, J. J. & Scherman, O. A. Quantitative multiplexing with nano-self-assemblies in SERS. *Sci. Rep.* **4,** 6785 (2015).
115. Di Martino, G. *et al.* Tracking Nanoelectrochemistry Using Individual Plasmonic Nanocavities. *Nano Lett.* **17,** 4840–4845 (2017).
116. Hoener, B. S. *et al.* Spectral Response of Plasmonic Gold Nanoparticles to Capacitive Charging: Morphology Effects. *J. Phys. Chem. Lett.* **8,** 2681–2688 (2017).
117. Cortés, E. *et al.* Plasmonic hot electron transport drives nano-localized chemistry. *Nat. Commun.* **8,** 14880 (2017).
118. Sun, M., Zhang, Z., Zheng, H. & Xu, H. In-situ plasmon-driven chemical reactions revealed by high vacuum tip-enhanced Raman spectroscopy. *Sci. Rep.* **2,** 647 (2012).
119. van Schrojenstein Lantman, E. M., Deckert-Gaudig, T., Mank, A. J. G., Deckert, V. & Weckhuysen, B. M. Catalytic processes monitored at the nanoscale with tip-enhanced Raman spectroscopy. *Nat. Nanotechnol.* **7,** 583–586 (2012).
120. Ding, T., Mertens, J., Lombardi, A., Scherman, O. A. & Baumberg, J. J. Light-Directed Tuning of Plasmon Resonances via Plasmon-Induced Polymerization Using Hot Electrons. *ACS Photonics* **4,** 1453–1458 (2017).
121. Peyronel, T., Quirk, K. J., Wang, S. C. & Tiecke, T. G. Luminescent detector for free-space optical communication. *Optica* **3,** 787 (2016).
122. Bogdanov, S. *et al.* Electron spin contrast of Purcell-enhanced nitrogen-vacancy ensembles in nanodiamonds. *Phys. Rev. B* **96,** 035146 (2017).
123. Davoyan, A. R. & Atwater, H. A. Purcell Enhancement of Parametric Luminescence: Bright and Broadband Nonlinear Light Emission in Metamaterials. (2017).